Enhanced Transient Angle Stability Control of Grid-Forming Converter Based on Virtual Synchronous Generator

Chen, Meng; Zhou, Dao; Blaabjerg, Frede

Published in:
I E E E Transactions on Industrial Electronics

DOI (link to publication from Publisher):
10.1109/TIE.2021.3114723

Publication date:
2022

Document Version
Accepted author manuscript, peer reviewed version

Enhanced Transient Angle Stability Control of Grid-Forming Converter Based on Virtual Synchronous Generator

Meng Chen, *Student Member, IEEE*, Dao Zhou, *Senior Member, IEEE*, and Frede Blaabjerg, *Fellow, IEEE*

***Abstract*—Attributed to the ability of inertia provision and good regulation performance, the virtual synchronous generator (VSG) has been proven as a promising solution to the problems introduced by using converter interfaced generation. Although the small-signal stability control of the VSG has been widely analyzed, the transient characteristics still needs more study, which belongs to a large-signal problem. In this paper, the transient angle stability control of the VSG is investigated. Two possible VSG emulation methods, i.e., the power-emulation and the torque-emulation, are compared from the perspective of transient characteristics. Then, the transient of the VSG internal voltage and its impact on the transient angle stability are quantitatively studied in details. Thereafter, an enhanced VSG controller is proposed, where a large-signal analysis is also presented to evaluate its influence on the acceleration and deceleration areas. Finally, the analysis and effectiveness of the enhanced VSG method are validated by the experimental results.**

***Index Terms*—Virtual synchronous generator, large-signal stability, transient angle stability, acceleration and deceleration areas, synchronous generator emulation**

I. Introduction

THE converter interfaced generators (CIGs) are quite different from the synchronous generators (SGs) in both the structure and control. On one hand, they are lack of physical inertia, which is helpful to stabilize the operation of the power system. Even though several kinds do have rotating elements like the wind turbine generators, their dynamics and the power system are decoupled by the static power converters [1]. On the other hand, the CIGs may have different control strategies, which directly determine the performance of the CIGs. Generally, the CIGs can be controlled in a grid-following way or a grid-forming way, which are suitable to different applications [2]. The grid-following way makes the CIGs as the controlled current sources, which synchronize to the power grid usually via the phase-locked loop (PLL) [3], [4]. It is the general choice when the CIGs are connected to a strong grid and try to inject powers by maximum power point tracking. It is because the grid-following control has high bandwidth and can achieve quick power tracking [5]. However, if the connected power grid is weak, the grid-following control may endure instability and lose the synchronization due to its high sensitivity to disturbance, which has been reported by both small-signal [6] and large-signal [7] analysis. In this context, the grid-forming control can be used, which behaves as a controlled voltage source and therefore enable the CIGs to establish the frequency and voltage by themselves without relying on a strong grid. It should be mentioned that the grid-forming converters always need some energy buffer, regardless of energy forms, in order to well fulfill their functions.

There are several kinds of proposed grid-forming CIGs, in which the virtual synchronous generator (VSG) is a promising solution [8]. The favorable features of an SG as well as its governor and automatic voltage regulator (AVR) are embedded in the control of a VSG, which makes the CIGs to have the abilities of inertia provision, frequency and voltage regulation. Nevertheless, a VSG is not exactly an SG after all, where its stability characteristics need special investigations. Meanwhile, the CIGs are much more flexible than the SGs, which leads to the possibility to improve the stability from the control perspective.

Among the stability problems of the power system, the angle stability is one of the key aspects. In general, the angle stability can be further divided into the small-signal and the transient angle stability [9]. Thanks to the well-established tools based on linear system theory such as eigenvalues and frequency analysis, the small-signal stability of the VSG have been widely investigated from different aspects, such as the small-signal dynamics [10]–[12], its differences with SGs [13], the modeling and parameters design [14]–[16], novel VSGs with improved small-signal stability [17], [18], etc. In comparison, the large-signal related transient angle stability of the VSG is limited studied, but important.

Due to the large currents, a typical way to deal with the transient of the VSG is triggering the current limits and switching the control mode to grid-following using the PLL. This issue is well studied in [19]. However, the scenario that the current limits are not triggered has drawn attention recently, especially in the weak grid. On one hand, the fault currents in the weak grid are not so high as in the strong grid due to the large line impedance. On the other hand, the VSG is also expected to keep the operation mode for a while from the stability of the power grid in the future. For example, in IEEE Std 1547-2018, it is recommended that the CIGs should not decrease the output active power for at least 10 s as the grid voltage drops to 0.5-0.8 p.u. [20], [21]. A comprehensive

The authors are with the AAU Energy, Aalborg University, Aalborg, 9220, Denmark (e-mail: mche@energy.aau.dk).

study of the transient angle stability of the grid-forming CIGs can be found in [22], which highlights that the VSG may undertake a angle instability due to its large virtual inertia even though there is a potential equilibrium after a large disturbance such as a grid voltage sag. Besides, the impact of the virtual governor and AVR has also been investigated in [23] and [24], respectively. Their results show that the small time constants in the virtual governor and AVR have opposite effects on the transient angle stability of the VSG. Although the negative influence of the virtual AVR is revealed in [23], the analysis is simply qualitative. In addition to the transient analysis, several methods are proposed to improve the angle stability of the VSG as well [21], [23]–[28]. A nonlinear controller is a potential choice to deal with the large-signal behavior, which is used in [25]. However, the control algorithm is complicated due to many nonlinear processes simultaneously applying to the power, frequency, and angle. A similar problem is found in the method of [26], where a mode detection block highly increases the complexity of the controller. In [27], the center of inertia (COI) is used to improve the transient stability of the VSG. Nevertheless, the COI has to be obtained from a central controller, which makes the method suffer from the drawbacks of a central control structure such as single-point failure. A much simpler method is proposed in [23] based on a voltage feedback. However, the added feedback signal changes the steady-state droop characteristics because the voltage does not always equal to its nominal value. Inspired from a similar idea, several literatures such as [24], [28], and [21] use the frequency signal instead of the voltage to improve the transient angle stability of the VSG. Although the PLL can restore the additional signal back to zero without influencing the steady-state droop characteristics, the dependence on the PLL may not be expected in practice.

This paper focuses on the transient angle stability problem of the grid-connected VSG controlled as a grid-forming converter when connected to a weak grid. Compared with the aforementioned works, the main contributions of this paper are summarized as follows.

1) Two used emulation methods of VSG, i.e., the power-form and the torque form, are compared from the transient point of view.
2) The transient dynamics of the internal voltage are investigated in detail, where some key problems such as its dynamic curve, monotonicity, and impact on the transient angle stability are quantitatively analyzed and proved.
3) A simple method by changing the acceleration and deceleration areas is proposed to enhance the transient angle stability of the VSG, which neither changing the steady-state droop characteristics nor relying on additional signal process such as the central controller, the PLL, etc.

The remainder of this paper is organized as follows. The transient angle stability analysis of the VSG including a comparison of emulation methods and the quantitative analysis of the internal voltage is given in Section II. In Section III, an enhanced VSG control is proposed to improve the transient angle stability, where a large-signal analysis is investigated as well. Section IV presents experimental results, and Section V draws the conclusions.

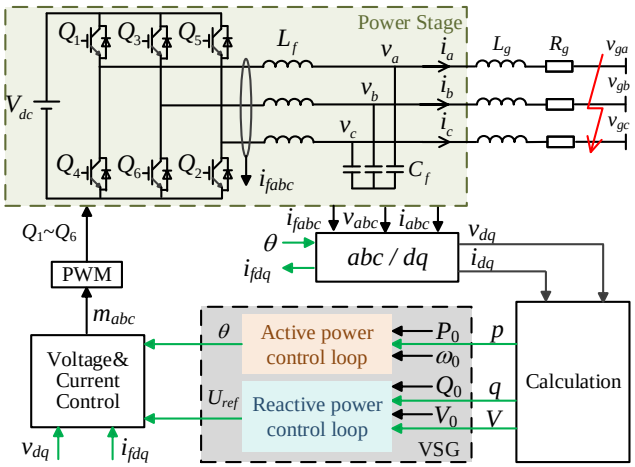

Fig. 1. General topology and control blocks of VSG.

II. Transient Angle Stability Analysis of VSG

Fig. 1 shows the general topology and control blocks of a VSG, where the power stage consists of a three-phase inverter and an *LC* filter, and the control structure mainly includes an active power control loop and a reactive power control loop. L_f and C_f are the filter inductor and capacitor, v_{abc} and i_{abc} are the three-phase output voltages and currents of the VSG, L_g and R_g are the line inductor and resistor to the infinite bus, where the three-phase voltages are v_{gabc}. The studied large-signal disturbance is a symmetrical three-phase-to-ground voltages drop at the infinite bus. The control system is based on the local *d*-*q* reference frame. The active power and reactive power control loops of the VSG will generate the voltage and angle of the internal voltage, i.e., U_{ref} and θ, respectively. The inner voltage and current control loops with quick dynamics are used to keep v_{abc} tracking the internal voltage of the VSG.

In the following, the impact of both the active and reactive power loops of the VSG on the transient angle stability will be studied in detail.

A. Comparison of two types of emulation methods

The active power control loop of the VSG emulates the swing equation of an actual SG to provide the virtual inertia and the governor to frequency regulation. In a p.u. system, its mathematical equation can be expressed as [10]

$$2H\dot{\omega} = P_0 - p - \frac{1}{D_p}(\omega - \omega_0) \tag{1}$$

$$\dot{\theta} = \omega_n \omega \tag{2}$$

where P_0 and ω_0 are the active power and frequency set-points, p and ω are the actual output active power and frequency of the VSG, ω_n is the base value of the frequency, H is the inertia constant, and D_p is the droop coefficient of the virtual governor. The system of (1), which describes the relationship between p and ω, is a simple linear system. Therefore, (1) has been widely used, which, in this paper, is called the power-form. Several literature involving the large-signal stability

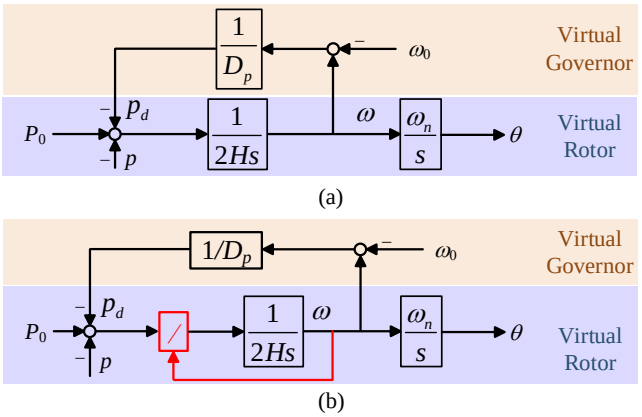

Fig. 2. Block diagram of active power control loop in Fig. 1. (a) Power-form. (b) Torque-form.

analysis are based on the power-form as well such as [22], [28], and [21]. The corresponding control block is shown in Fig. 2(a).

For an SG, the power-form is a simplification when $\omega \approx 1$ p.u. It is especially reasonable in the small-signal analysis. If a closer emulation of an SG is preferred, the torque-form should be used, which is given as [12]

$$2H\dot{\omega} = T_m - T \tag{3}$$

where T_m and T are the input and output torques, respectively. It should be mentioned that all the control system in this paper is established in the p.u. system. Therefore, H in both (1) and (3) are identical and it is not necessary to consider the difference in the unit between power and torque [29]. By combining with the governor and replacing the torques by the active powers, (3) can be rewritten as

$$2H\omega\dot{\omega} = P_0 - p - \frac{1}{D_p}(\omega - \omega_0) \tag{4}$$

As seen, the dynamics between p and ω become nonlinear and ω may have different influence during the transient compared with that in (1). The block diagram of the torque-form is shown in Fig. 2(b). It should be mentioned that, the torque-form is also used in several papers such as in [23] and [24], while they do not study the differences compared with the power-form responding to a large-signal disturbance. In the following, such differences will be investigated.

The studied system is assumed to be pure inductive in this paper. On one hand, a virtual reactance is usually used to make it inductive if the system is resistive [10]. Otherwise, the active power is mainly related to the voltage. Then the performance of the VSG will be influenced, which uses active power to control the frequency. On the other hand, as claimed in [21], the line resistor has benefits to the transient stability by increasing the maximum power transfer capability and variation range of the power angle. Therefore, the worst condition of $R_g = 0$ is considered. By applying a symmetrical three-phase-to-ground voltages drop and neglecting the governor, the power angle

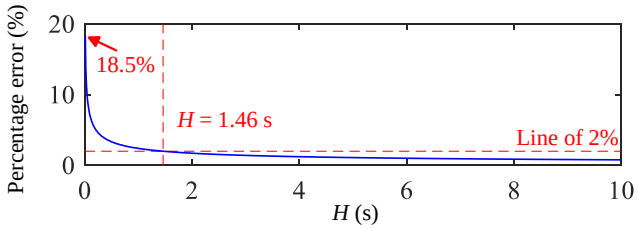

Fig. 3. Maximum percentage error of δ between two inertia emulation forms when H increases from 0.01 s to 10 s.

dynamics of the power-form and torque-form can be derived, respectively, as

$$\ddot{\delta} = \frac{\omega_n}{2H}P_0 \tag{5}$$

$$\ddot{\delta}\dot{\delta} + \omega_n\omega_g\ddot{\delta} = \frac{\omega_n^2}{2H}P_0 \tag{6}$$

where δ is defined as

$$\dot{\delta} = \omega_n\omega - \omega_n\omega_g \tag{7}$$

Solving (5) and (6) gives the trajectories of δ controlled by different emulation forms as

$$\delta = \delta_0 + \frac{\omega_n P_0}{4H}t^2 \tag{8}$$

$$\delta = \delta_0 + \frac{2H\omega_n}{3P_0}(\omega_g^2 + \frac{P_0}{H}t)^{3/2} - \omega_n\omega_g t - \frac{2H\omega_n}{3P_0}\omega_g^3 \tag{9}$$

where δ_0 is the initial power angle. As seen, the error of δ between the power-form and the torque-form is related to H. For an SG, H is constant at a relative large value, which makes this error small, while for a VSG, H can be flexibly chosen as a small value of several milliseconds such as [30] or as large as several seconds such as [11]. Fig. 3 shows the maximum percentage error of δ between the two emulation methods when H changes between 0.01-10 s. Other necessary parameters are based on Table I, where the nominal values are chosen as the base to calculted p.u. values and the connected grid is weak with the short-circuit ratio (SCR) being 1.9. The time constant of the active power control loop, i.e., $2HD_p$, is around 1.6 s to well behave the inertia. D_p and H are chosen based on their typical orders of magnitude according to [22], [26], [28]. Fig. 3 implies that, after the disturbance, ω controlled by the power-form will have larger deviations, which lead δ to increase to a larger value than that of the torque-form via a same duration of time. On the contrary, the torque-form has better transient characteristics with slower increasing speed and smaller deviation of ω than the power-form. When H is large enough, their maximum difference is small. However, when H is smaller than 1.46 s, this difference is larger than 2% and can quickly increase to almost 20% with $H = 0.01$ s. Therefore, the two emulation methods are similar when using a large H, while the VSG with torque-form is beneficial with a small H being used. It should be mentioned that the error will be further decreased if the function of the governor is included.

B. Effects of internal voltage on transient angle stability

The aforementioned analysis does not take the variation of the internal voltage U_{ref} into consideration, which is in

TABLE I
PARAMETERS USED IN EXPERIMENTS

Symbol	Description	Value
ω_n	nominal frequency	100π rad/s
S_n	nominal power	1 kW
V_n	nominal line-to-line RMS voltage	80 V
ω_g	grid frequency	1 p.u.
V_g	grid voltage	1 p.u.
L_g	line inductor	0.52 p.u.
P_0	set-point value of active power	1 p.u.
ω_0	set-point value of frequency	1 p.u.
V_0	set-point value of voltage	1.01 p.u.
Q_0	set-point values of reactive power	0 p.u.
D_p	droop coefficient of virtual governor	0.09 p.u.
H	inertia constant	9 s
D_q	droop coefficient of virtual AVR	0.05 p.u.
k_q	integral gain of virtual AVR	110 p.u.

accordance with a typical analysis for an SG. In the context of a VSG, U_{ref} may behave with distinct dynamics. In [23], it has been initially revealed that considering the variation of U_{ref} can deteriorate the transient stability of a VSG. However, the analysis is simple and qualitative. Therefore, this paper will evaluate the effects of U_{ref} comprehensively.

A typical block diagram of the reactive power control loop, i.e., virtual AVR, is shown in Fig. 4, where the internal voltage of the VSG is derived by

$$U_{ref} = k_q \int (V_0 + D_q Q_0 - V - D_q q) dt \tag{10}$$

where V_0 and Q_0 are the voltage and reactive power set-points, V and q are the output voltage and reactive power of the VSG, D_q is the droop coefficient of the reactive power control loop, and k_q is an integral gain. It is worth mentioning that, the following two simplifications are applied to (10):

1) As a typical way to simplify the analysis, the dynamics of the internal voltage and current loops are neglected due to their quick response [15], [22], [26]. As a result, there is $V = U_{ref}$, where (10) is rewritten as

$$U_{ref} = (V_0 + D_q Q_0 - D_q q)\frac{k_q}{s + k_q} \tag{11}$$

which is equal to the basic droop control with a low-pass filter (LPF) and the time constant is $1/k_q$.

2) As shown in Table I, $k_q = 110$ is used in this paper. The time constant is about 0.01 s (typical value is from several milliseconds to tens of milliseconds [31], [32]), which is much smaller than the angle dynamics (in most applications, the time scale of the angle dynamics of the VSG is at least hundreds of milliseconds due to the virtual inertia). Therefore, the dynamics of the filter is neglected as well just like [23], [28]. The reactive power control in (11) is further simplied to

$$V_0 + D_q Q_0 - U_{ref} - D_q q = 0 \tag{12}$$

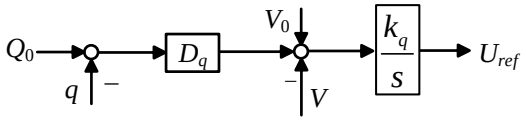

Fig. 4. Block diagram of the reactive power control loop in Fig. 1.

In addition, p and q of the VSG can be expressed as

$$p = \frac{V_g U_{ref} sin\delta}{X_g} \tag{13}$$

$$q = \frac{U_{ref}(U_{ref} - V_g \cos\delta)}{X_g} \tag{14}$$

where V_g is the magnitude of the grid voltage. By combining (12)-(14), the relationship among p, U_{ref}, and δ can be derived as

$$U_{ref} = \frac{\sqrt{(D_q V_g \cos\delta - X_g)^2 + 4D_q X_g (V_0 + D_q Q_0)}}{2D_q} + \frac{D_q V_g \cos\delta - X_g}{2D_q} \tag{15}$$

$$p = \frac{V_g sin\delta \sqrt{(D_q V_g \cos\delta - X_g)^2 + 4D_q X_g (V_0 + D_q Q_0)}}{2D_q X_g} + \frac{D_q V_g^2 \sin\delta\cos\delta - X_g V_g \sin\delta}{2D_q X_g} \tag{16}$$

Using (15), it can further be investigated how U_{ref} changes with δ. To this end, an intermediate variable can be defined as

$$m = \frac{D_q V_g \cos\delta - X_g}{2D_q}, \quad \delta \in [0, \pi] \tag{17}$$

which yields

$$U_{ref} = \sqrt{m^2 + \frac{X_g(V_0 + D_q Q_0)}{D_q}} + m \tag{18}$$

The derivative of U_{ref} with respect to m is

$$\frac{dU_{ref}}{dm} = 1 + \frac{m}{\sqrt{m^2 + X_g(V_0 + D_q Q_0)/D_q}} > 0 \tag{19}$$

which means that U_{ref} is a monotonically increasing function of m. Meanwhile, the monotonicity of m with respect to δ and V_g can be derived by

$$\frac{\partial m}{\partial \delta} = -\frac{V_g}{2}\sin\delta \le 0 \tag{20}$$

$$\frac{\partial m}{\partial V_g} = \frac{1}{2}\cos\delta \begin{cases} \ge 0, & \delta \in [0, \pi/2] \\ < 0, & \delta \in (\pi/2, \pi] \end{cases} \tag{21}$$

which implies, combining with (19), that U_{ref} is monotonically decreasing as δ increases, and the monotonicity of U_{ref} with V_g is based on δ. When $\delta \in [0, \pi/2]$, U_{ref} is monotonically decreasing as the sag depth of V_g increases, while the corresponding relationship is opposite when $\delta \in (\pi/2, \pi]$. Substitute $\delta = \pi/2$ into (15) yields

$$\alpha := U_{ref}(\frac{\pi}{2}) = \frac{\sqrt{X_g^2 + 4D_q X_g (V_0 + D_q Q_0)}}{2D_q} - \frac{X_g}{2D_q} \tag{22}$$

which is a constant without influenced by V_g.

Fig. 5 shows both of the curves of p-δ and U_{ref}-δ with different depths of voltage sag. It should be mentioned that, the virtual governor is neglected in this part. As shown in (1), if considering the virtual governor, the actual input power can be seen as $P_0 - 1/D_p(\omega - \omega_0)$, which is time-varying based on ω and will make the analysis complicated. Fortunately, the virtual governor always provide a damping and tends to restrain the variation of ω. Therefore, the common strategy in the analysis of both traditional SG and VSG is to neglect its function and consider the worse case without damping. Thereafter, the input power is assumed to be only P_0, which is constant [26], [29]. Nevertheless, in the following discussion on the $\delta - \omega$ trajectory, the impact of the virtual governor will be included. Normally, the equilibrium point a is a stable operation point with U_{ref} being U_0. When the grid voltage drops to, e.g., 0.6 p.u., the operation point is changed to c. Due to the power unbalance, there is $\dot{\omega} > 0$, which enlarges δ from δ_0 to δ_d. It is noted that U_{ref} will also drop from U_0 to U_c at the moment of V_g disturbance. Thus the p-δ curve is lower than the one with a constant U_0, which implies a larger acceleration area. On the p-δ curve, there is $\delta_d > \delta'_d$. Once the operation point goes across point d, δ increases continuously while $\dot{\omega} < 0$. If ω can return to the grid frequency before point e, the system can finally reach to the new stable equilibrium point d. Otherwise, the system is unstable. It is noted that, after the drop from U_0 to U_c, U_{ref} is not kept at U_c. When δ increases from δ_0 to δ_e, the operation point on the U_{ref}-δ curve moves from point c_1 to point e_1 leading U_{ref} gradually decreasing from U_c to U_e. This decrease will further lower the p-δ curve as δ increases. Then two results can be expected as shown in the p-δ curve. Firstly, the maximum power point appears earlier than the point $\delta = \pi/2$ such as from p_{max} to p'_{max}. Secondly, there is $(\delta'_e - \delta_e) > (\delta_d - \delta'_d)$, which implies that the impacts of U_{ref} on the acceleration area and deceleration area are different. Although the variations of U_{ref} can simultaneously enlarge the acceleration area and lessen the deceleration area, the latter is more obviously. In the following, it will be shown that this conclusion is related to the depth of the voltage sag. Further comparing the curves with different depth of the voltage sag can give some more detailed findings. As shown in Fig. 5, at $\delta = \delta_0$, when V_g drops to 0.8 p.u. and 0.6 p.u., there is $U_c < U_b < U_0$. However, at $\delta = \delta_e$, the effects are opposite, i.e., $U_e > U_f > U_g$. The boundary angle is $\delta = \pi/2$, where U_{ref}, as in (22), is α. Furthermore, considering a small voltage sag from point a_1 to b_1, there are $U_b \approx U_0$ and $(U_0 - U_b) \ll (U_0 - U_h)$. Therefore, as the aforementioned conclusion, the variations of U_{ref} have more impact on the deceleration area than the acceleration area. Meanwhile, the smaller the voltage sag is, the more obvious the difference of the impact is. For a small voltage sag of the grid, the variations of U_{ref} can hardly change the acceleration area. However, the deceleration area may be significantly decreased. This distinction on the acceleration and deceleration areas will be less when the voltage sag becomes deeper because the curves of U_{ref}-δ become flatter.

Fig. 6 further shows the trajectories of the system in the δ-ω plane and the dynamics of U_{ref} with different grid voltage

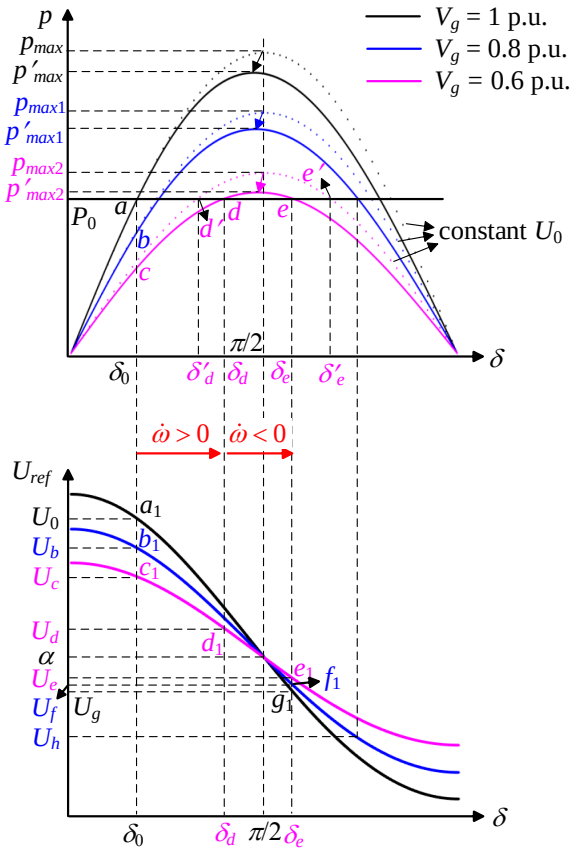

Fig. 5. p-δ curve and U_{ref}-δ curve with different voltage sags.

sags. The effects of the governor are also considered. As the used inertia constant is large, the emulation of the power-form is used. The initial equilibrium point is $(\delta, \omega) = (\delta_0, 1)$. Once V_g drops to 0.8 p.u., ω is increased by the unbalanced power, which leads δ to increase as well. If assuming U_{ref} is constant at U_0, δ will maximally reach to δ_1, where ω returns back to 1 p.u. again. Thereafter, the system will achieve a new stable operation point. However, due to the decrease of U_{ref} as shown in Fig. 6(b), δ will actually reach to δ_2, which is larger than δ_1. It implies that the dynamics of U_{ref} decrease the stable margin, which makes the system more easily entering instability. Nevertheless, the system is still stable. In comparison, in the case that V_g drops to 0.6 p.u., δ is increased to as large as δ_3 and then gradually stabilized at δ'_d when U_{ref} is assumed as constant, which indicates a stable system. However, the actual U_{ref} severely drops, which leads ω still to be larger than 1 p.u. even though δ reaches the critical power angle δ_e. Thereafter, the system goes into instability. In summary, the dynamics of U_{ref} will deteriorate the stability of VSG and may even cause the system to be unstable after a large disturbance.

III. Enhanced Large-Signal Angle Stability Control Method

A. Proposed control method

The aforementioned analysis shows that it may be possible to improve the large-signal stability of a VSG by proper

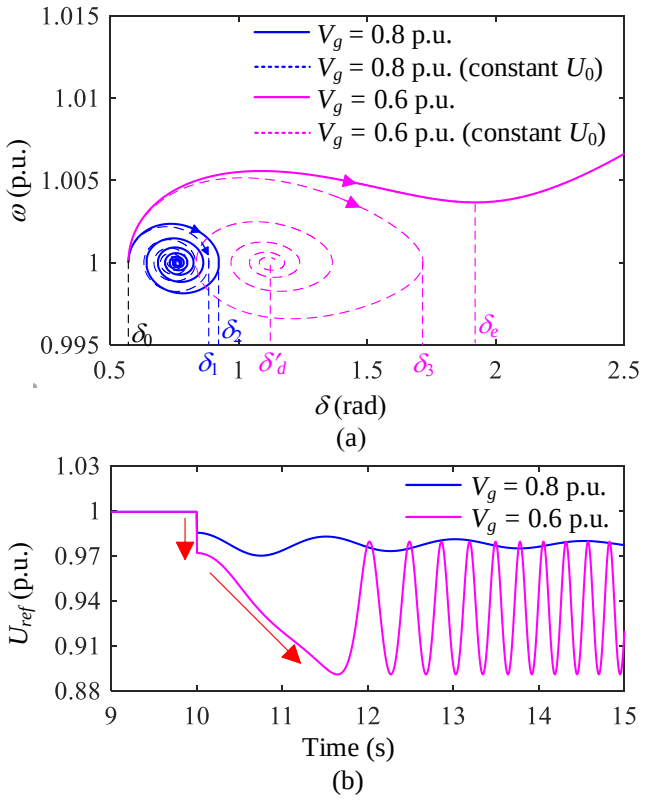

Fig. 6. Effects of U_{ref} with different voltage sags. (a) Trajectories in δ-ω plane. (b) Time-domain waveform of U_{ref}.

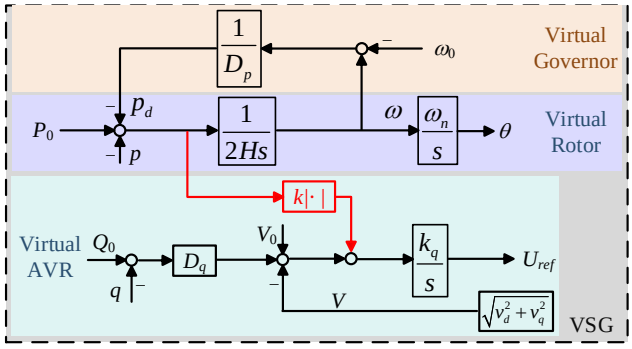

Fig. 7. Enhanced large-signal angle stability control method of virtual synchronous generator (VSG).

control of U_{ref}. Meanwhile, it is expected that the steady-state q-V droop relationship is not changed. Since the angle disturbance is always with a power unbalance, an enhanced large-signal angle stability control method is proposed as shown in Fig. 7, in which U_{ref} is derived as

$$U_{ref} = k_q \int (V_0 + D_q Q_0 - V - D_q q + 2Hk|\dot{\omega}|)dt \tag{23}$$

where $k \geq 0$ is a control gain.

It is noted that $\dot{\omega}$ is naturally obtained from the active power control loop, where no additional derivative calculator is needed. With the proposed control method, the relationship between U_{ref} and δ is changed to

$$U_{ref} = \begin{cases} f_1(\delta), & p \leq P_0 \\ f_2(\delta), & p > P_0 \end{cases} \tag{24}$$

where

$$f_1(\delta) = n + \sqrt{n^2 + \frac{X_g}{D_q}(V_0 + D_q Q_0 + kP_0)} \tag{25}$$

$$f_2(\delta) = n' + \sqrt{n'^2 + \frac{X_g}{D_q}(V_0 + D_q Q_0 - kP_0)} \tag{26}$$

$$n = \frac{D_q V_g \cos\delta - X_g - kV_g \sin\delta}{2D_q} \tag{27}$$

$$n' = \frac{D_q V_g \cos\delta - X_g + kV_g \sin\delta}{2D_q} \tag{28}$$

B. Large-signal stability analysis

The purpose of this section is to prove that, with the proposed method, the large-signal stability of the VSG can be improved by decreasing the potential acceleration area and increasing the available deceleration area. Before that, as mentioned above, the steady-state droop characteristics is not supposed to be changed, thus it firstly shows that the new system has and only has the identical equilibria with the original system.

Proof 1): From (23), the dynamics of U_{ref} with the proposed method is

$$\dot{U}_{ref} = k_q(V_0 + D_q Q_0 - V - D_q q + 2Hk|\dot{\omega}|) \tag{29}$$

Set the right-hand-side of (1) and (29) to zero

$$2H\dot{\omega} = P_0 - p - \frac{1}{D_p}(\omega - \omega_0) = 0 \tag{30}$$

$$\dot{U}_{ref} = k_q(V_0 + D_q Q_0 - V - D_q q + 2Hk|\dot{\omega}|) = 0 \tag{31}$$

which yields the same equation with (12). Therefore, the system with the proposed method shares the identical equilibria with the original system. As shown in Fig. 5, point a is the shared stable equilibrium before the voltage sag. Similarly, point d is the shared stable equilibrium when V_g drops to 0.6 p.u. while point e is an unstable equilibrium.

Then it will show that: $\forall\ \delta \in (0,\pi)$, there is $p(k>0) \geq p(k=0)$ and the equal sign works if and only if $\delta = \delta_d$ or $\delta = \delta_e$.

Proof: For a given $\delta \in (0,\pi)$, according to (13) and (24), the derivate of p with respect to k is

$$\frac{dp}{dk} = \begin{cases} \dfrac{V_g \sin\delta}{X_g}\left(\dfrac{X_g P_0 - V_g n \sin\delta}{2D_q\sqrt{n^2 + X_g/D_q(V_0 + D_q Q_0 + kP_0)}} - \dfrac{V_g \sin\delta}{2D_q}\right), & p \leq P_0 \\ \dfrac{V_g \sin\delta}{X_g}\left(\dfrac{V_g n' \sin\delta - X_g P_0}{2D_q\sqrt{n'^2 + X_g/D_q(V_0 + D_q Q_0 - kP_0)}} + \dfrac{V_g \sin\delta}{2D_q}\right), & p > P_0 \end{cases} \tag{32}$$

Besides, from (24) and (26), there are

$$\sqrt{n^2 + \frac{X_g}{D_q}(V_0 + D_q Q_0 + kP_0)} = U_{ref} - n, \quad p \leq P_0 \tag{33}$$

$$\sqrt{n'^2 + \frac{X_g}{D_q}(V_0 + D_q Q_0 - kP_0)} = U_{ref} - n', \quad p > P_0 \tag{34}$$

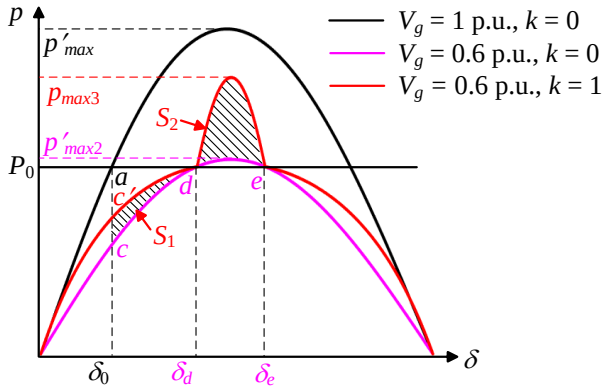

Fig. 8. p-δ curve with the proposed method.

Placing (33) and (34) into (32) yields

$$\frac{dp}{dk}=\begin{cases}\dfrac{V_g\sin\delta(X_gP_0-V_gU_{ref}sin\delta)}{2X_gD_q\sqrt{n^2+X_g/D_q(V_0+D_qQ_0+kP_0)}}, & p\le P_0\\ \dfrac{V_g\sin\delta(V_gU_{ref}sin\delta-X_gP_0)}{2X_gD_q\sqrt{n'^2+X_g/D_q(V_0+D_qQ_0-kP_0)}}, & p>P_0\end{cases} \tag{35}$$

which can be further simplified, based on (13), to be

$$\frac{dp}{dk}=\begin{cases}\dfrac{V_g\sin\delta(P_0-p)}{2D_q\sqrt{n^2+X_g/D_q(V_0+D_qQ_0+kP_0)}}\ge 0, & p\le P_0\\ \dfrac{V_g\sin\delta(p-P_0)}{2D_q\sqrt{n'^2+X_g/D_q(V_0+D_qQ_0-kP_0)}}>0, & p>P_0\end{cases} \tag{36}$$

By combining the cases of $p\le P_0$ and $p>P_0$ together, there is

$$\frac{dp}{dk}\ge 0 \tag{37}$$

which implies that p is a monotonically increasing function of k, i.e.,

$$p(k>0)\ge p(k=0) \tag{38}$$

where the equal sign works only if $p=P_0$. Meanwhile, it has been proved that the system with the proposed method has the same equilibria with the original system, i.e., point d and point e in Fig. 5. Therefore, the equal sign works only if $\delta=\delta_d$ or $\delta=\delta_e$.

Based on the aforementioned analysis, the new p-δ curve with the proposed method is shown in Fig. 8. Due to (38), the p-δ curve at $\delta=\delta_0$ with $k=1$ is higher than the original one (i.e., $k=0$) when V_g drops to 0.6 p.u. Therefore, the operation point is improved to point c'. Afterwards, δ is increased to δ_e, where the new system and the original system share the same equilibrium. Thus, the potential acceleration area is decreased by S_1. Similarly, when δ enlarges from δ_d to δ_e, the potential deceleration area will be increased by S_2. To sum up, the large-signal angle stability is expected to be improved by the proposed VSG control method.

C. Design and Effects of control parameter

For the design of transient stability, the traditional loci-based or frequency-based small-signal analysis is not reasonable, while an iterative algorithm [21], [33] can be used to determine the limitation of control parameter k. The procedure is summarized as following:

1) Initialization. According to the large-signal analysis above, the basic requirement for k is $k\ge 0$. Thus $k=0$ is chosen as the initial value.
2) Equilibrium calculation. Let the active power in (16) be the set-point value P_0, where the equilibrium δ_e is derived.
3) Trajectory calculation. The typical numerical integration [23], [29] is used to get the trajectory of δ and U_{ref} based on (1), (7), (13), (14), (29).
4) First Decision. If $\delta>\delta_e$, $k=k+0.01$, and go back to 3). If $\delta\le\delta_e$, $k_{min}=k$, this process is disabled and go on to 5).
5) Second Decision. It is convenient to set an upper limitation for U_{ref} in case of a severe over modulation, e.g., $U_{ref}\le 1.2$ is used in this paper. If it is met, $k=k+0.01$, and go back to 3). Otherwise, $k_{max}=k-0.01$, and go on to 6).
6) Output k_{min} and k_{max}.

Accordingly, the available region of k in this paper is $k\in[0.54,0.94]$ p.u. It should be mentioned that when k is out of this region, the proposed method is still have impact. Nevertheless, when $k<0.54$, the impact is not strong enough to bring the system back to stable. When $k>0.94$, the controller may reach saturation, which implies that the effective k will be smaller than the used value. However, this smaller effective k can still decrease the potential acceleration area and increase the potential deceleration area to improve the large-signal angle stability.

Fig. 9 shows the new system trajectories in δ-ω plane with different k when applying the new proposed method. The case $k=0$ represents the original system controlled by the traditional VSG, which has been shown as unstable in Fig. 6(a). When $k=0.3$, the frequency deviation during the transient is decreased. However, the system is still unstable. It is noticed that, in this case, the critical power angle is slightly decreased from δ_e to δ_{en}. This is because the analysis based on p-δ curve such as in Fig. 8 neglects the droop terms. The impact of the virtual governor on the critical power angle can be explained by using Fig. 10. As aforementioned before, when the virtual governor is neglected, the input power is constant at P_0, where the critical angle is δ_{ee}. When considering the virtual governor, the actual input power is determined by the droop characteristics. From Fig. 9, when δ reaches to the critical value, there is $\omega_e>\omega_0$, which makes the input power decreases to $P_0-1/D_p(\omega_e-\omega_0)<P_0$. Then the critical power angle with the virtual governor δ_e is larger than δ_{ee} as in Fig. 10. Then further with $k=0.3$, the proposed method makes ω to be smaller, i.e., $\omega_{en}<\omega_e$ in Fig. 9. As a result, there is $P_0-1/D_p(\omega_e-\omega_0)<P_0-1/D_p(\omega_{en}-\omega_0)$. According to Fig. 10, the new critical power angle will become smaller to δ_{en}. When $k=0.6$, ω can return to 1 p.u. when δ increases to δ_4, which is smaller than the critical power angle. Thereafter, the system is gradually stabilized at a new

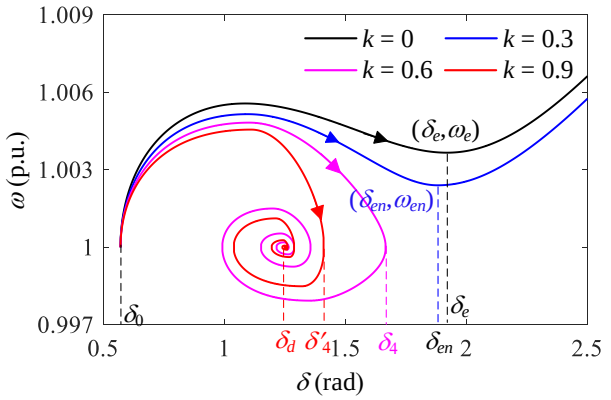

Fig. 9. New trajectories in δ-ω plane with different k when applying the proposed method.

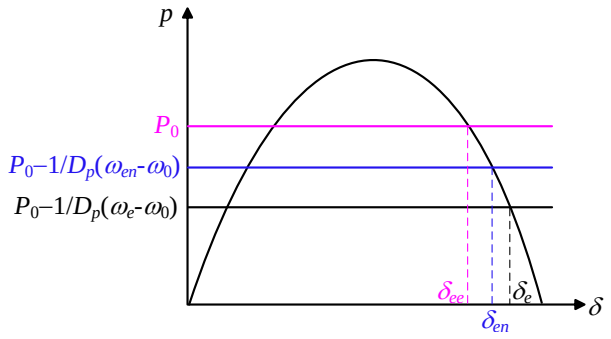

Fig. 10. Impact of virtual governor on input power and critical power angle.

state $(\delta, \omega) = (\delta_d, 1)$, which demonstrates the effectiveness of the proposed method. As k continuously increases to 0.9, both of the maximum deviations of δ and ω are decreased. Especially, the maximum angle deviation is obviously limited by the proposed method.

D. Comparison with other methods

Several methods have been proposed to improve the large-signal angle stability of the VSG [21], [23]–[28]. In [26] and [21], these methods are commented from different aspects. This paper also gives some comparisons between the proposed method and several similar methods in the literature, where the results are summarized in Table II. Firstly, a method is better to be simple and local-information-based in practice. In [25], a nonlinear damping method based on the back-stepping design is proposed, which, therefore, is complicated in the implementation. A center of inertia based method is proposed in [27] to make the control structure slightly simpler. However, it is still complex due to the dependence on a central information. Secondly, the steady-state droop regulation characteristics is not supposed to be changed. From this point of view, although the method in [23] is simple, the used additional signal may not be zero in the steady-state due to the error of voltage. In contrast, the PLL is used in [21], [24], [28] to provide both a simple and zero-additional-signal control. However, these methods will inevitably introduce the PLL-related instability especially when there is a frequency disturbance from the grid.

TABLE II
COMPARISON OF VSGS WITH IMPROVED LARGE-SIGNAL ANGLE STABILITY

Methods	Simplicity	Steady-state regulation	PLL-free	Local information
[25], [26]	x	√	√	√
[27]	x	√	√	x
[23]	√	x	√	√
[21], [24], [28]	√	√	x	√
Proposed method	√	√	√	√

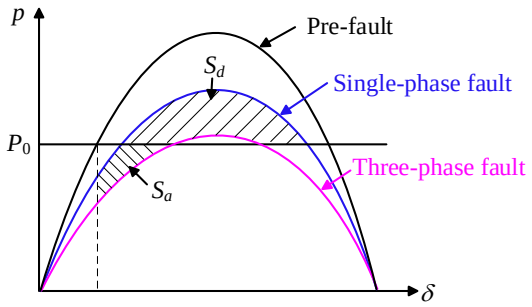

Fig. 11. Comparisons of p-δ curves between three-phase and single-phase faults.

It should be mentioned that it is usually difficult to find a method with all benefits, which implies that a compromise is necessary. For example, although the methods in [25]–[27] are more complex in implementation than others, they may provide better performance in some cases theoretically.

E. Applications to unbalanced faults and single-phase system

Although the proposed method is based on the three-phase symmetrical system, it is of potential use in responding to the unbalanced faults or the single-phase system by small changes.

The severity of the voltage drop is related to the equivalent fault reactance, which can be calculated by using the symmetrical components. The smaller the equivalent fault reactance is, the more severe the fault is. It has been proven that the three-phase voltage drop is the most severe one [29]. Fig. 11 compares the p-δ curves of the three-phase and the single-phase voltage drops, which shows the former has a larger acceleration area than the latter by S_a but a smaller deceleration area by S_d. Therefore, this paper take the most severe three-phase voltage drop as the case study. Nevertheless, the proposed method is also useful to the single-phase voltage drop because the principle of the proposed method is by changing the acceleration and deceleration areas as shown in Fig. 8.

The proposed method can also be applied to the single-phase system, where the instantaneous powers of the VSG is not constant but have double-frequency oscillations. The second-order generalized integrator quadrature signal generator (SOGI-QSG) can be used to derive the average powers, i.e., $\overline{p}$ and $\overline{q}$ [34]. Therefore, the proposed control of the VSG

can be changed by replacing the instantaneous values p and q to $\overline{p}$ and $\overline{q}$, i.e.,

$$2H\dot{\omega} = P_0 - \overline{p} - \frac{1}{D_p}(\omega - \omega_0) \tag{39}$$

$$U_{ref} = k_q \int (V_0 + D_q Q_0 - V - D_q \overline{q} + 2Hk|\dot{\omega}|)dt \tag{40}$$

Thereafter, all the relationships with respect to the instantaneous powers in the three-phase system are identical with those in the single-phase system using the average powers as shown in [35]. Thus, the transient angle stability can be improved by the proposed method.

IV. Experimental Results

To validate the effectiveness of the proposed method, the experiments are carried out with the topology shown in Fig. 1, where Fig. 12 shows the experimental setup. The power inverter is based on the Danfoss drive system, and a Chroma 61845 grid simulator is used as the connected power grid. The filter currents i_{fabc}, output voltages v_{abc} and currents i_{abc} are measured and sent to dSPACE DS1007 platform via DS2004 A/D Board. The control algorithm is coded in a personal computer and loaded via a patch cable to be implemented by dSPACE DS1007. Then the DS5101 digital waveform output board is used to generate the PWM signals to drive the inverter. Besides, the data in dSPACE DS1007 is also sent to the PC to display the waveforms via the patch cable. The important outputs, i.e., angle frequency ω, active power p, and voltage magnitude V can be directly measured from the control system. The power angle δ is measured by $\theta - \theta_g$, where θ_g is the angle of the grid measured by PLL. It should be mentioned that the PLL is only used to get the waveform of δ, but does not participate in the control during the operation. The used parameters are given in Table I.

Before evaluating the impact of the internal voltage and the proposed method, Fig. 13 compares the dynamics responding to the drop to 0.6 p.u. of V_g between power-form and torque-form emulations with small inertia and damping by setting $H = 0.05$ and $D_p = 1.3$. In accordance with the analysis, the torque-form gives a slower variation of ω. Meanwhile, the difference is small at the beginning. It is because the analysis in Section II assumes the damping is zero and V_g decreases to 0 in order to derive the analytical solutions [29]. In the experiment, the damping from D_p, the parasitic resistors of the setup, and the remained V_g will decrease their difference. Nevertheless, the conclusion of the analysis is not influenced.

Fig. 14 and Fig. 15 are used to verify the analysis about the internal voltage E_f. Fig. 14 shows the experimental results using the traditional VSG when V_g drops to 0.6 p.u. Due to the voltage drop during the transient, the traditional VSG has worse large-signal angle stability, where the system is unstable. It should be mentioned that although the former analysis simplifies (11) to (12), in the experiments, the original control structure is used without simplification. The quick dynamics of the voltage can be observed in Fig. 14, which also verifies that the time scale is small enough compared with the angle transient and the simplication in the analysis is reasonable. In contrast, if the droop characteristics is disabled, where the

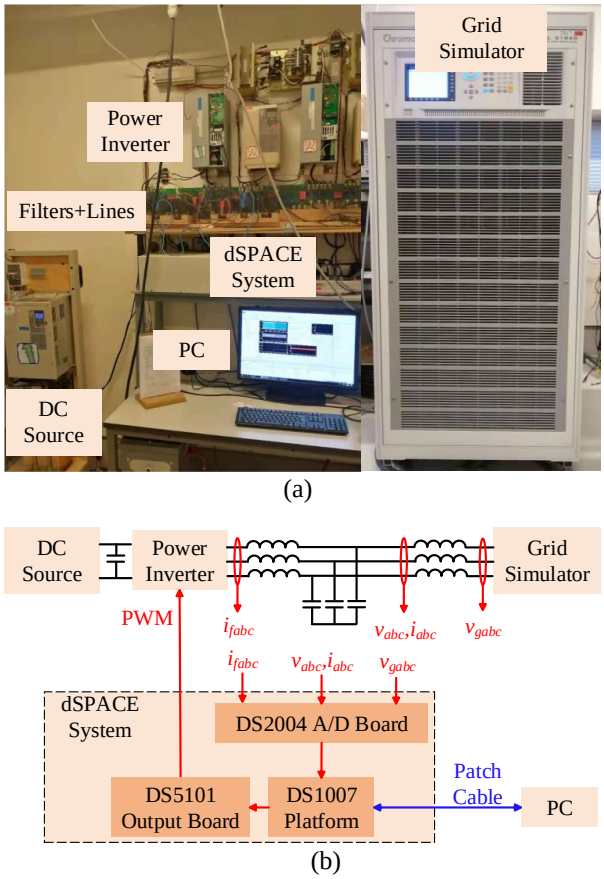

Fig. 12. Experimental setup of VSG. (a) Physical Picture. (b) Configuration.

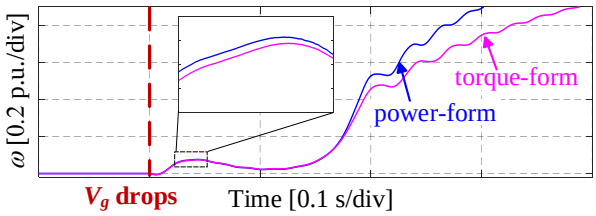

Fig. 13. Comparisons between power-form and torque-form emulations with small inertia and damping.

experimental results are shown in Fig. 15, the system can be gradually stable after some oscillations following the same large-signal disturbance.

Fig. 16 provides the experimental results with the proposed method following the same V_g sag to 0.6 p.u., where $k = 0$ represents the results with the traditional VSG control as presented in Fig. 14. As shown, with either $k = 0.6$ or $k = 0.9$, the large-signal angle stability of the system is improved. Meanwhile, compared with $k = 0.6$, the system has smaller maximum frequency and angle deviations when $k = 0.9$. It is worth noting that the oscillation attenuation is not significantly changed, which implies that the damping is not added. It proves therefore that the principle of the proposed method to improve the large-signal angle stability is providing a simple way to change the acceleration and deceleration areas.

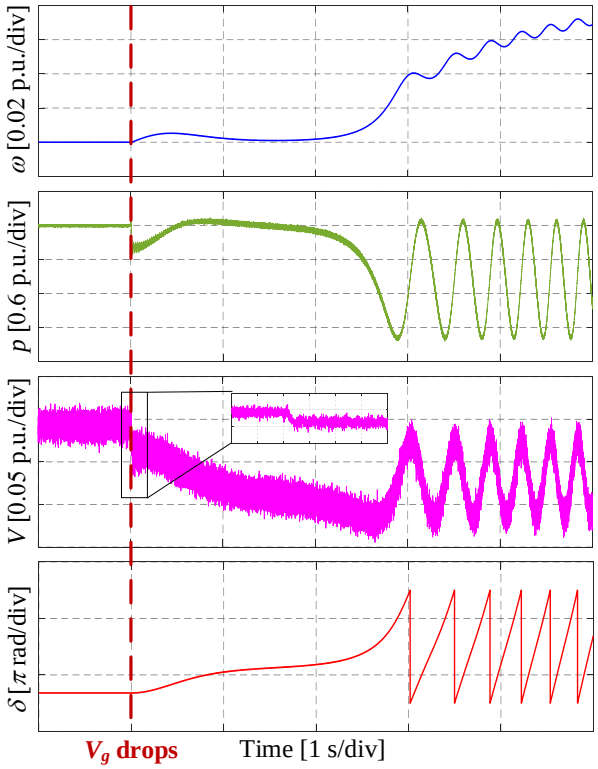

Fig. 14. Experimental results of traditional VSG when V_g drops to 0.6 p.u.

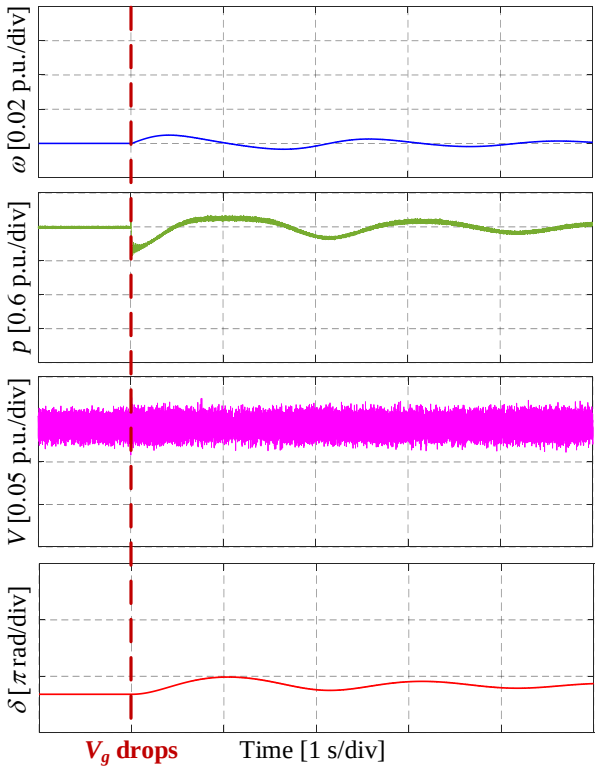

Fig. 15. Experimental results of traditional VSG when V_g drops to 0.6 p.u. without virtual AVR.

V. Conclusion

This paper has investigated the large-signal angle stability of the VSG-based grid-forming converters. It firstly shows that the torque-form emulation has a better stability compared to the power-form emulation in a low inertia and damping condition, where their distinctions will decrease as the inertia increases. Then, the negative effects of the terminal voltage dynamics are quantitatively revealed in detail. Finally, a method to enhance the large-signal angle stability of the VSG is proposed and verified. The results conclude that although the proposed method cannot increase the damping of the system, it provides a simple way to improve the large-signal angle stability by changing the acceleration and deceleration areas.

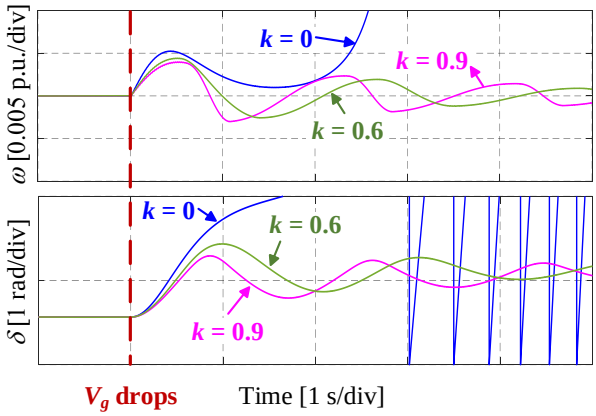

Fig. 16. Experimental results of proposed method with different controller gains k when V_g drops to 0.6 p.u.

References

[1] J. Fang, H. Li, Y. Tang, and F. Blaabjerg, "On the inertia of future more-electronics power systems," *IEEE J. Emerg. Sel. Top. Power Electron.*, vol. 7, no. 4, pp. 2130–2146, Dec. 2019.

[2] J. Rocabert, A. Luna, F. Blaabjerg, and P. Rodríguez, "Control of power converters in AC microgrids," *IEEE Trans. Power Electron.*, vol. 27, no. 11, pp. 4734–4749, Nov. 2012.

[3] D. Pan, X. Ruan, X. Wang, H. Yu, and Z. Xing, "Analysis and design of current control schemes for LCL-type grid-connected inverter based on a general mathematical model," *IEEE Trans. Power Electron.*, vol. 32, no. 6, pp. 4395–4410, Jun. 2017.

[4] W. Du, F. Tuffner, K. P. Schneider, R. H. Lasseter, J. Xie, Z. Chen, and B. P. Bhattarai, "Modeling of grid-forming and grid-following inverters for dynamic simulation of large-scale distribution systems," *IEEE Trans. Power Deliv.*, 2020.

[5] L. Huang, H. Xin, and F. Dörfler, "H_∞ control of grid-connected converters: Design, objectives and decentralized stability certificates," *IEEE Trans. Smart Grid*, vol. 11, no. 5, pp. 3805–3816, Sep. 2020.

[6] X. Wang, L. Harnefors, and F. Blaabjerg, "Unified impedance model of grid-connected voltage-source converters," *IEEE Trans. Power Electron.*, vol. 33, no. 2, pp. 1775–1787, 2018.

[7] X. Fu, J. Sun, M. Huang, Z. Tian, H. Yan, H. H.-C. Iu, P. Hu, and X. Zha, "Large-signal stability of grid-forming and grid-following controls in voltage source converter: A comparative study," *IEEE Trans. Power Electron.*, vol. 36, no. 7, pp. 7832–7840, Jul. 2021.

[8] M. Chen, D. Zhou, and F. Blaabjerg, "Modelling, implementation, and assessment of virtual synchronous generator in power systems," *J. Mod. Power Syst. Clean Energy*, vol. 8, no. 3, pp. 399–411, May 2020.

[9] Power System Dynamic Performance Committee, "Stability definitions and characterization of dynamic behavior in systems with high penetration of power electronic interfaced technologies," Tech. Rep., 2020.

[10] Y. Hirase, K. Abe, K. Sugimoto, K. Sakimoto, H. Bevrani, and T. Ise, "A novel control approach for virtual synchronous generators to suppress frequency and voltage fluctuations in microgrids," *Appl. Energy*, vol. 210, pp. 699–710, Jan. 2018.

[11] W. Du, Q. Fu, and H. F. Wang, "Power system small-signal angular stability affected by virtual synchronous generators," *IEEE Trans. Power Syst.*, vol. 34, no. 4, pp. 3209–3219, Jul. 2019.

[12] Z. Wang, H. Yi, F. Zhuo, J. Wu, and C. Zhu, "Analysis of parameter influence on transient active power circulation among different generation units in microgrid," *IEEE Trans. Ind. Electron.*, vol. 68, no. 1, pp. 248–257, Jan. 2021.

[13] M. Chen, D. Zhou, and F. Blaabjerg, "Characteristics of virtual synchronous generator based voltage source converter," in *Proc. 2020 IEEE Power Energy Soc. Gen. Meet.*, 2020, pp. 1–5.

[14] S. D'Arco, J. A. Suul, and O. B. Fosso, "Small-signal modeling and parametric sensitivity of a virtual synchronous machine in islanded operation," *Int. J. Electr. Power Energy Syst.*, vol. 72, pp. 3–15, Nov. 2015.

[15] H. Wu, X. Ruan, D. Yang, X. Chen, W. Zhao, Z. Lv, and Q.-C. Zhong, "Small-signal modeling and parameters design for virtual synchronous generators," *IEEE Trans. Ind. Electron.*, vol. 63, no. 7, pp. 4292–4303, Jul. 2016.

[16] O. Mo, S. D'Arco, and J. A. Suul, "Evaluation of virtual synchronous machines with dynamic or quasi-stationary machine models," *IEEE Trans. Ind. Electron.*, vol. 64, no. 7, pp. 5952–5962, Jul. 2017.

[17] S. A. Khajehoddin, M. Karimi-Ghartemani, and M. Ebrahimi, "Grid-supporting inverters with improved dynamics," *IEEE Trans. Ind. Electron.*, vol. 66, no. 5, pp. 3655–3667, May 2019.

[18] J. Liu, Y. Miura, H. Bevrani, and T. Ise, "A unified modeling method of virtual synchronous generator for multi-operation-mode analyses," *IEEE J. Emerg. Sel. Top. Power Electron.*, vol. 9, no. 2, pp. 2394–2409, Apr. 2021.

[19] H. Wu and X. Wang, "Design-oriented transient stability analysis of PLL-synchronized voltage-source converters," *IEEE Trans. Power Electron.*, vol. 35, no. 4, pp. 3573–3589, Apr. 2020.

[20] IEEE Standard Association, *IEEE Std. 1547-2018. Standard for Interconnection and Interoperability of Distributed Energy Resources with Associated Electric Power Systems Interfaces*, 2018.

[21] X. Xiong, C. Wu, D. Pan, and F. Blaabjerg, "An improved synchronization stability method of virtual synchronous generators based on frequency feedforward on reactive power control loop," *IEEE Trans. Power Electron.*, vol. 36, no. 8, pp. 9136–9148, 2021.

[22] D. Pan, X. Wang, F. Liu, and R. Shi, "Transient stability of voltage-source converters with grid-forming control: A design-oriented study," *IEEE J. Emerg. Sel. Top. Power Electron.*, vol. 8, no. 2, pp. 1019–1033, Jun. 2020.

[23] Z. Shuai, C. Shen, X. Liu, Z. Li, and Z. J. Shen, "Transient angle stability of virtual synchronous generators using Lyapunov's direct method," *IEEE Trans. Smart Grid*, vol. 10, no. 4, pp. 4648–4661, Jul. 2019.

[24] H. Cheng, Z. Shuai, C. Shen, X. Liu, Z. Li, and Z. J. Shen, "Transient angle stability of paralleled synchronous and virtual synchronous generators in islanded microgrids," *IEEE Trans. Power Electron.*, vol. 35, no. 8, pp. 8751–8765, Aug. 2020.

[25] M. Ashabani and Y. A.-R. I. Mohamed, "Integrating VSCs to weak grids by nonlinear power damping controller with self-synchronization capability," *IEEE Trans. Power Syst.*, vol. 29, no. 2, pp. 805–814, Mar. 2014.

[26] H. Wu and X. Wang, "A mode-adaptive power-angle control method for transient stability enhancement of virtual synchronous generators," *IEEE J. Emerg. Sel. Top. Power Electron.*, vol. 8, no. 2, pp. 1034–1049, Jun. 2020.

[27] M. Choopani, S. H. Hosseinian, and B. Vahidi, "New transient stability and LVRT improvement of multi-VSG grids using the frequency of the center of inertia," *IEEE Trans. Power Syst.*, vol. 35, no. 1, pp. 527–538, Jan. 2020.

[28] X. Xiong, C. Wu, B. Hu, D. Pan, and F. Blaabjerg, "Transient damping method for improving the synchronization stability of virtual synchronous generators," *IEEE Trans. Power Electron.*, vol. 36, no. 7, pp. 7820–7831, Jul. 2021.

[29] J. Machowski, J. W. Bialek, and D. J. Bumby, *Power System Dynamics: Stability and Control*. Wiley, 2011.

[30] R. Rosso, S. Engelken, and M. Liserre, "Robust stability analysis of synchronverters operating in parallel," *IEEE Trans. Power Electron.*, vol. 34, no. 11, pp. 11 309–11 319, Nov. 2019.

[31] S. D'Arco, J. A. Suul, and O. B. Fosso, "A virtual synchronous machine implementation for distributed control of power converters in smartgrids," *Electr. Power Syst. Res.*, vol. 122, pp. 180–197, May 2015.

[32] X. Meng, J. Liu, and Z. Liu, "A generalized droop control for grid-supporting inverter based on comparison between traditional droop control and virtual synchronous generator control," *IEEE Trans. Power Electron.*, vol. 34, no. 6, pp. 5416–5438, Jun. 2019.

[33] T. Shintai, Y. Miura, and T. Ise, "Oscillation damping of a distributed generator using a virtual synchronous generator," *IEEE Trans. Power Deliv.*, vol. 29, no. 2, pp. 668–676, Apr. 2014.

[34] J. A. Suul, S. DArco, and G. Guidi, "Virtual synchronous machine-based control of a single-phase bi-directional battery charger for providing vehicle-to-grid services," *IEEE Trans. Ind. Appl.*, vol. 52, no. 4, pp. 3234–3244, Jul. 2016.

[35] H. Li, X. Zhang, T. Shao, and T. Q. Zheng, "Flexible inertia optimization for single-phase voltage source inverter based on hold filter," *IEEE J. Emerg. Sel. Top. Power Electron.*, vol. 7, no. 2, pp. 1300–1310, Jun. 2019.

Meng Chen (Graduate Student Member, IEEE) received the B.Eng. degree in electrical engineering from Qingdao University of Science and Technology, Qingdao, China, in 2013. Since 2013, he was a Postgraduate Student with North China Electric Power University, Beijing, China. He was a visiting scholar with Aalborg University, Denmark and Swiss Federal Institute of Technology Zurich (ETH Zurich), Switzerland, in 2017 and 2021, respectively. He is currently pursuing the Ph.D. degree in power electronics with Aalborg University, Denmark. His research interest is the application of power electronics in the power grid.

He is a recipient of the 2020 MPCE Best Paper Award.

Dao Zhou (Senior Member, IEEE) received the B.S. from Beijing Jiaotong University, Beijing, China, in 2007, the M. S. from Zhejiang University, Hangzhou, China, in 2010, and the Ph.D. from Aalborg University, Aalborg, Denmark, in 2014, all in electrical engineering. Since 2014, he has been with Department of Energy Technology, Aalborg University, where currently he is an Associate Professor. His research interests include modeling, control, and reliability of power electronics in renewable energy applications.

He serves as an Associate Editor for IET Renewable Power Generation and IET Power Electronics. He also received a few IEEE prized paper awards.

Frede Blaabjerg (Fellow, IEEE) was with ABB-Scandia, Randers, Denmark, from 1987 to 1988. He got the PhD degree in Electrical Engineering at Aalborg University in 1995. He became an Assistant Professor in 1992, an Associate Professor in 1996, and a Full Professor of power electronics and drives in 1998. From 2017 he became a Villum Investigator. He is honoris causa at University Politehnica Timisoara (UPT), Romania and Tallinn Technical University (TTU) in Estonia.

His current research interests include power electronics and its applications such as in wind turbines, PV systems, reliability, harmonics and adjustable speed drives. He has published more than 600 journal papers in the fields of power electronics and its applications. He is the co-author of four monographs and editor of ten books in power electronics and its applications.

He has received 33 IEEE Prize Paper Awards, the IEEE PELS Distinguished Service Award in 2009, the EPE-PEMC Council Award in 2010, the IEEE William E. Newell Power Electronics Award 2014, the Villum Kann Rasmussen Research Award 2014, the Global Energy Prize in 2019 and the 2020 IEEE Edison Medal. He was the Editor-in-Chief of the IEEE TRANSACTIONS ON POWER ELECTRONICS from 2006 to 2012. He has been Distinguished Lecturer for the IEEE Power Electronics Society from 2005 to 2007 and for the IEEE Industry Applications Society from 2010 to 2011 as well as 2017 to 2018. In 2019-2020 he served as a President of IEEE Power Electronics Society. He has been Vice-President of the Danish Academy of Technical Sciences. He is nominated in 2014-2020 by Thomson Reuters to be between the most 250 cited researchers in Engineering in the world.